SEQUENTIAL SILICON SURFACE MELTING AND ATMOSPHERIC PRESSURE PHOSPHORUS DOPING FOR CRYSTALLINE TUNNEL JUNCTION FORMATION IN SILICON/PEROVSKITE TANDEM SOLAR CELLS

G. Gaspar[1], J. C. Cardoso[1], I. Costa[1], A. Guerra[1], A. S. Viana[2], M. E. M. Jorge[2], D. Vilhena[1], D. Pera[1], J. A. Silva[1], A. M. Vallêra[1], L. Vines[3], J. M. Serra[1], K. Lobato[1]
[1]Instituto Dom Luiz (IDL), Faculdade de Ciências da Universidade de Lisboa, Campo Grande, 1749-016 Lisboa, Portugal
[2]Centro de Química Estrutural, Faculdade de Ciências da Universidade de Lisboa, Campo Grande, 1749-016 Lisboa, Portugal
[3]Department of Physics, Centre for Materials Science and Nanotechnology, University of Oslo, N-0316 Oslo, Norway

ABSTRACT: In monolithically integrated 2-terminal silicon/perovskite tandem solar cells, one of the critical steps is the formation of the layer(s) that interconnects the two sub-cells. Of the range of possibilities for monolithic integration, crystalline silicon tunnel junctions are a potential candidate. The crystalline tunnel junction has the advantage of transparency whilst also withstanding high temperature steps which may be required to form the perovskite sub-cell on top of the silicon sub-cell.
Here, we present our recent scalable setup that has its core based on the gas immersion laser doping technique (GILD). We have adapted it to reach high speed rastering of the laser spot over large areas to dope silicon wafers with the aim of forming a tunnel junction, i.e. shallow doping with an abrupt doping profile.
Morphological analysis of the laser processed samples after parameters tuning has resulted in the unequivocal shallow melting while faceted structures are left to solidify on the surface. Shallow phosphorus depth profiles (< 1 µm) with an abrupt concentration drop were also measured in the processed samples. We observed that the number of scans has a predominate impact on the profiles' form.

Keywords: Tandem Solar Cells; c-Si Tunnel Junction; Laser Doping

1 INTRODUCTION

The efficiency limited single junction solar cell solely based on crystalline silicon (c-Si) wafers is currently considered one of the main hurdles in driving PV electricity generation costs down. This can be overcome if a tandem architecture is used as complementary parts of the solar spectrum can be absorbed by each sub-cell [1]. These can be connected in a monolithic architecture (two terminals), using, normally, a recombination layer, or in a stacked architecture (four terminals), where there is a transparent and insulating layer between the two sub-cells. It can be argued that monolithic tandem cells are a more promising approach for the future of solar cells, since they present lower power losses and potentially lower production costs [2]. Nowadays, most tandem cells use non-scalable or/and high cost techniques (e.g. PECVD, Ion Implantation, etc.) to produce such layer, usually reffered to as a recombination layer or tunnel junction [3,4].

In any case, this interconnection layer should avoid significant electrical and optical losses and minimize the trade-offs necessary for the perovskite top sub-cell, e.g. it should preferentially withstand high temperatures, which is unlikely when amorphous Si is used [5].

We apply the gas immersion laser doping technique (GILD), which is the process of doping a semiconductor by surrounding it with a dopant gas and then using ns laser pulses to melt the surface and hence allow the doping gas to diffuse into the melt before recrystallization [6]. Because diffusion occurs in the molten phase of the Si, the required high doping densities and abrupt differences in doping level for tunnel junctions are possible. Here, GILD has been adapted to include high speed rastering of the laser spot over large wafer-scale areas. With the cost reduction, power efficiency and flexibility provided by modern laser systems, doping depth profile control associated to large area processing, suggests that this approach for the formation of wafer scale tunnel junctions as being one with industrial relevance.
In this paper, a phosphorous n^{++} doping strategy, based on an atmospheric pressure laser doping system, has been developed. The phosphorus depth profiles, as measured via secondary ion mass spectrometry (SIMS), demonstrate the viability of this process for the ultra-shallow doping of Si with potential to be employed in the production of Si tunnel junctions.

2 EXPERIMENTAL

In order to have a setup that is industrially attractive, we have designed a setup to operate at slight overpressure, which is imposed by the designed inert gas system. A reaction chamber coupled to an IR-transparent window, and operating at room temperature, was designed to accomodate 10 x 10 cm^2 samples. The chamber is coupled to a bubbler that contains the liquid phosphorous precursor ($POCl_3$). We used this fuming liquid phosphorus source since it has been extensively used over the past years in the solar cell industry in the formation of emitters on p-type Si base wafers [7,8]. In our specific case, the Ar atmosphere at 1.05 bar was saturated with $POCl_3$ (vapor partial pressure of 0.037 bar at 293 K [9,10]). We maintanined an Ar flow passing through the $POCl_3$ bubbling system until the reaction chamber pressure equals. A solid-state pumped laser operating at 1064 nm wavelength is then used as the local heating source for the Si surface melting. Fig. 1a) shows the simplified process flow for the doping of the wafers.

Here, the pulse rate and the energy density were fixed at 500 kHz and ca 10.5 J/cm^2, respectively. Attention was devoted to the impact of scan speed (v) on the surface morphology and the resulting doping profiles of the samples. It was varied from 500 to 5000 mm/s with the aim of fast surface processing. v can be converted to

distance between consecutive pulses (p), which will be further used in the interpretation of the results. A wide range of other laser parameters were explored, namely the spacing between adjacent scanned lines (d) and number of times that the same area is scanned (n). For practical reasons, the surface morphology analysis was carried out on samples that were produced according to the process flow in Fig. 1a) but using only Ar as the chamber atmosphere. To better visualize the developed doping process, a schematic of the reaction chamber with Si wafer immersed into $POCl_3$-rich atmosphere while irradiated is shown in Fig. 1b).

2-inch p-type (100)-oriented monocrystalline Czochralski Si wafers, with average resistivity and thickness of 5 Ω·cm and 275 µm, respectively, were used as the base substrate. Mirror-like mechanically polished wafers were chosen to facilitate interpretation of the phenomenon of laser interaction with the surface as well as to better control the melting depth needed for a tunnel junction.

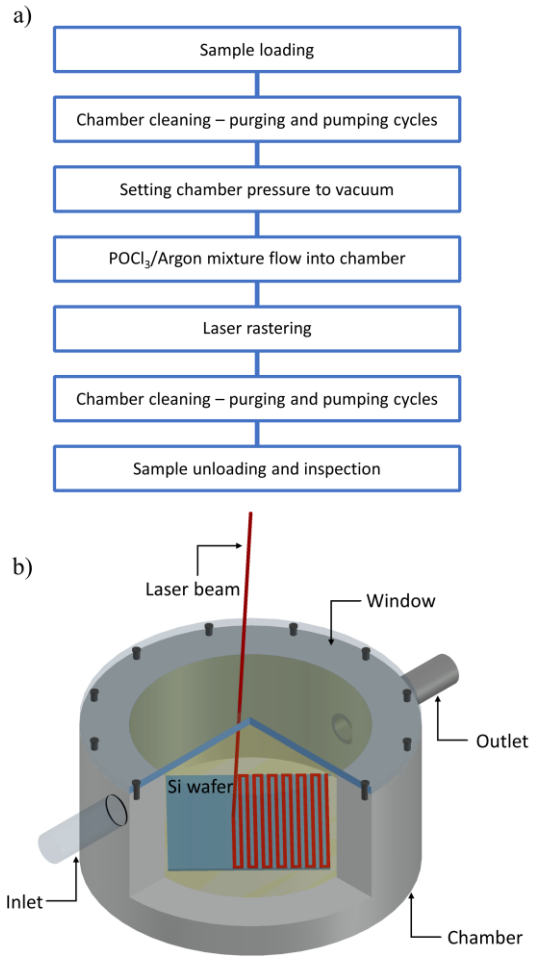

Figure 1: a) Simplified process flow for the laser doping setup. b) Reaction chamber, where the Si wafer is immersed in $POCl_3$-rich atmosphere while being laser irradiated.

3 RESULTS AND DISCUSSION

3.1 Laser melting and surface morphology

Field-Emission Scanning Electron Microscopy (FE-SEM) was used to inspect surface morphology. Fig. 2a) corresponds to a micrograph showing an individual laser scanned line processed at d = 40 µm and p = 2 µm, so that each line should not influence the nearest neighbors. It can be observed that the laser scanned line has a width of ca 22 µm, defining the spot diameter of interaction under the current lasing and Si surface conditions. This picture also indicates the unequivocal surface melting of Si. Given the order of magnitude of the laser pulse diameter employed, the heat diffusion becomes crucial to the volume of molten Si [11]. From the inset picture one can observe that part of the molten Si is released from the laser spot probably due to Marangoni forces present in the molten areas [12]. This suffers a further crystallization on the virgin Si (100)-oriented wafer areas that are present between two consecutive lines. The density and size of these structures should depend on the molten Si volume per pulse, local wetting of liquid on solid Si as well as the dissimilar density between the two phases [13, 14].

Fig. 2b) shows a higher magnification micrograph of the center of a processed line where d was reduced to 20 µm in order to fully process the wafers' surface. The sub-micrometer size bases of the dispersed pyramidal-like shape structures are clearly observed, which suggests a facet growth mechanism upon melt quenching, while they partially impinge with the nearest neighbors during recrystallization. Thus, two consecutive phenomena should take place leading to the final surface morphology of the samples: 1) Si depth melting during pulse dwell time, which was set to 220 ns in the present work; and 2) anisotropic molten Si released from the laser spot that further recrystallizes on the surface. Hence, the visible structures in the micrographs are possibly a result of the solidified Si on an already recrystallized surface during pulse dwell. If the spacing between adjacent lines is reduced to d = 10 µm, the size of the structures seems to increase while their density is fairly constant as shown in Fig. 2c). We have employed two rastering sequences under the same lasing settings, which lead to fully connected structures (Fig. 2d). By maintaining d as 10 µm, but increasing the pulse center interval distance to p = 3.5 µm, the morphology of the surface is similar to the one processed at p = 2 µm, as can be observed in Fig. 2e).

The distance between pulses was further increased to p = 4 µm, and the corresponding micrograph is shown in Fig. 2f). Here, the morphology of the surface seems to drastically change compared to the ones processed at lower p values, i.e. $p \leq 3.5$ µm. The surface is characterized by recrystallized crusts separated by ca 4 µm, which corresponds to the distance between pulses for the applied scan rate.

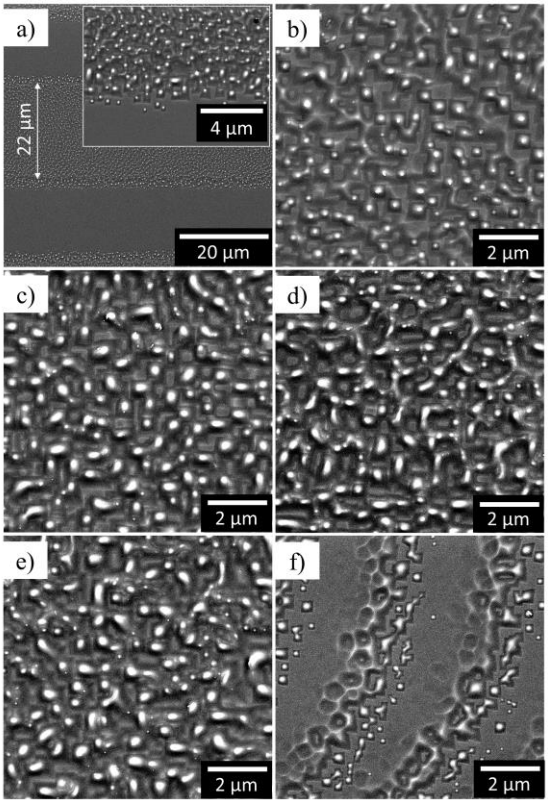

Figure 2: High-resolution FE-SEM micrographs of laser processed samples using: a) d = 40 µm, p = 2 µm and n = 1x; b) d = 20 µm, p = 2 µm and n = 1x; c) d = 10 µm, p = 2 µm and n = 1x; d) d = 10 µm, p = 2 µm and n = 2x; e) d = 10 µm, p = 3.5 µm and n = 1x; f) d = 10 µm, p = 4 µm and n = 1x. The inset in figure a) serves to highlight the pyramidal-like structures formed in the periphery of the laser spot boundaries.

Fig. 3 shows complementary Atomic Force Microscopy (AFM) measurements performed at the center of a laser scanned line in the corresponding processed areas, for an area of 5 x 5 µm^2. Here, all samples were processed at d = 10 µm, while a reference sample, i.e. without being laser processed, is also probed and the results shown in Fig. 3a). The root mean square (RMS) roughness extracted for the reference sample shows a fairly flat surface compared to laser processed ones, with a RMS below 1 nm. Fig. 3b) shows the topography mapping of sample processed
Looking closer at the topography of the spaces between crusts, it seems that the surface does not present the very same topography as in the reference one. This fact associated to what was already verified in Fig. 2a) and Fig. 2f) indicates that the surface underwent shallow melting, and the crusts are a consequence of the Marangoni forces and the released molten Si behind the laser beam while the surface is scanned. In this case, it seems that the surface melting/recrystallization may be also related to the limited lateral heat of diffusion [15]. It is expected that the diffusion length due to a single pulse leads to a thermal averaging over a certain distance. In this case, and assuming a thermal diffusivity of 0.1 cm^2/s for Si at its melting point [16], as well as a pulse width of 220 ns for the current laser, the thermal diffusion length corresponds to ca 1.5 µm, this being in the order of magnitude d employed in the present experiments.

When d decreases to 2 µm, the surface topography changes abruptly as shown in Fig. 3c). As mentioned before, the structures comprise pyramid-like structures with sharp edges, with a RMS nearly four times higher than the one verified for the sample processed at d = 4 µm. It is interesting to note that a second rastering results in a smoother surface as demonstrated by the reduction in its RMS to 18.1 nm. Fig. 3d) also shows that the structures are more variable in terms of dimensions, while small pyramidal-like structures seem also to grow from the walls of other larger ones. It should be noted that the structure base edges and heights are present in different dimension scales. Thus, the topography resulting from a second scan may be explained by the higher number of random interactions of the photons with the structures leading to the smoothening of the previously grown pyramids.

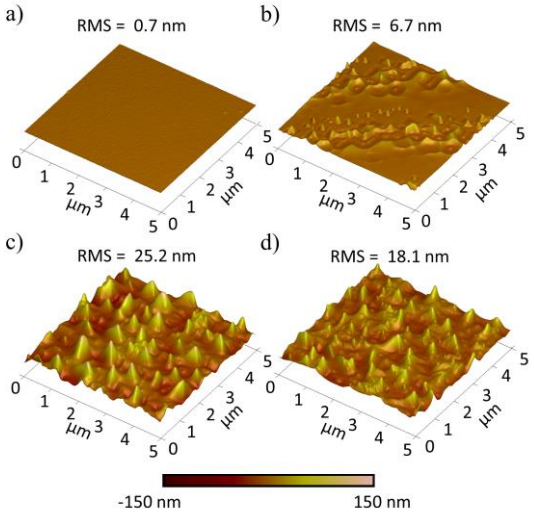

Figure 3: AFM 3D images of a) reference and processed sample surfaces comprising: b) p = 4 µm, n = 1x; c) p = 2 µm, n = 1x; and d) p = 2 µm, n = 2x.

3.2 Phosphorus doping profiles

Phosphorus depth profiles of laser doped samples were measured with SIMS using a Cs primary ion beam at 15 keV to sputter craters of 100 x 100 µm^2 while the data was obtained from a physical aperture of 8 µm diameter. The measured SIMS intensity was calibrated using implanted standards. Fig. 4 shows the corresponding phosphorus depth profile concentrations as obtained for samples processed at p = 2 µm and different number of rastering sequences, i.e. n = 1x, 2x and 3x. The depth profiles were measured until the deep shoulder was visualized. Also, a sample that was exposed to the saturated $POCl_3$ atmosphere, but without any thermal budget applied to its surface, was measured with SIMS. From the results it seems that there is some chemisorption/condensation of $POCl_3$ at the sample surface, reaching a thickness of ca 80 nm. We consider that until this depth there is no phosphorus incorporation into Si, and thus have added the dashed orange line to represent it.

The results clearly show that the peak dopant concentration in the layers depends on the number of laser-induced melting/solidification cycles, as it is possible to observe in the inset of the figure. For the last one, the values were obtained along the reference orange line. It is also observed that the number of scans leads to an increase in depth of the heavily doped layers, reaching ca 700 nm

for n = 3x, as it was already reported in literature for Si doping with boron [17]. It should be highlighted that the measured profiles may be overestimated in terms of depth due to geometric reasons as the surfaces present peak-to-valley heights in the order of tens of nanometers while the SIMS primary beam hits the surface with an angle of 30-50º off the sample normal. It is also possible that the incorporation of phosphorus depends on the chemisorption/condensation of $POCl_3$ at the surface prior laser rastering [18]. Indeed, the obtained peak concentrations are ca two orders of magnitude lower than the solid solubility limit of phosphorus in Si at temperatures above 1000 ºC [19]. Thus, we expect to be able to increase the concentration even higher using a larger number of scans and without having the formation of electrically inactive precipitates.

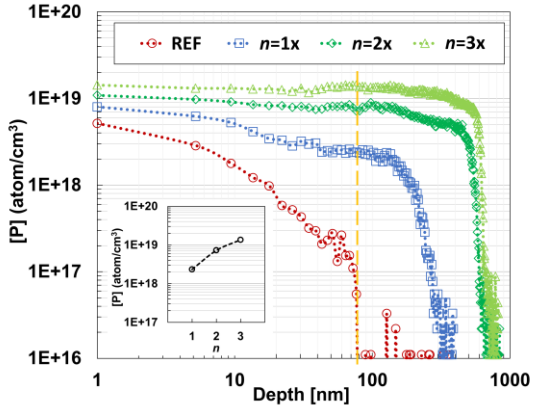

Figure 4: SIMS phosphorous depth profiles for unprocessed reference sample (red circles), and processed ones using d = 2 µm and n = 1x (blue squares), n = 2x (dark green diamonds) or n = 3x (light green triangles). The orange dashed line sets the phosphrous surface concentration effectively incorporated. The inset corresponds to the phosphrous concentrations along the mentioned line and as a function of n.

4 CONCLUSIONS

A compact setup was successfully developed to shallow dope Si wafers with phosphorous at the atmospheric pressure.

The morphological analysis of the processed Si samples shows laser shallow melting of the surface which is then followed by rapid solidification into pyramidal-like arrays.

SIMS depth profiling shows that both phosphorous doping depth and concentration profile depends on the laser processing parameters (e.g. number of scans) and potentially on $POCl_3$ adsorption at the surface.

Laser doping parameters must be further optimized to reach shallower n^{++} Si layers on the highly doped p^{++} Si while etch-back strategies will be also considered, if necessary.

REFERENCES

[1] Z. Yu, M. Leilaeioun, Z. Holman, Nature Energy 1 (2016) 16137.

[2] T. Todorov, O. Gunawan, S. Guha, Molecular Systems Design and Engineering 1 (2016) 370–376.

[3] F. Sahli, J. Werner, B.A. Kamino, M. Brauninger, R. Monnard, B. Paviet-Salomon, L. Barraud, L. Ding, J.J.D. Leon, D. Sacchetto, G. Cattaneo, M. Despeisse, M. Boccard, S. Nicolay, Q. Jeangros, B. Niesen, C. Ballif, Nature Materials 17 (2018) 820-826.

[4] F. Milési, M. Coig, J.F. Lerat, T. Desrues, J. Le Perchec, A. Lanterne, L. Lachal, F. Mazen, Nuclear Instruments and Methods in Physics Research B 409 (2017) 53-59.

[5] T. Mueller, J. Wong, A. G. Aberle, Energy Procedia 15 (2012) 97–106.

[6] G. Kerrien, J. Boulmer, D. Débarre, D. Bouchier, A. Grouillet, D. Lenoble, Applied Surface Science 186 (2002) 45–51.

[7] H. Ghembaza, A. Zerga, R. Saïm, M. Pasquinelli. Silicon Springer 10 (2018) 377-386.

[8] H. Li, K. Kim, B. Hoex, S. Wenham, M. Abbott, Frontiers in Energy 11 (2017) 42–51.

[9] D. R. Stull, Industrial & Engineering Chemistry 39 (1947) 518–536.

[10] National Institute of Standards and Technology, NIST Chemistry WebBook, SRD 69 (2020, September 10). https://webbook.nist.gov/cgi/cbook.cgi?ID=C10025873&Mask=4&Type=ANTOINE&Plot=on.

[11] T. Sameshima, Applied Physics A 96 (2009) 137-144.

[12] E. Haro-Poniatowski, C. Acosta-Zepeda, G. Mecalco, J. L. Hernández-Pozos, N. Batina, I. Morales-Reyes, J. Bonse, Journal of Applied Physics 115 (2014) 224309.

[13] W.-K. Rhim, K. Ohsaka, Journal of Crystal Growth 208 (2000) 313-321.

[14] X.-Y. Cui, S.P. Ringer, G. Wang, Z.H. Stachurski, The Journal of Chemical Physics 151 (2019) 194506.

[15] M. Gedvilas, S. Indrišiūnas, B. Voisiat, E. Stankevičius, A. Selskis, G. Račiukaitis, Physical Chemistry Chemical Physics 20 (2018) 12166-12174.

[16] H.R. Shanks, P.D. Maycock, P.H. Sidles, G.C. Danielson, Physical Review 130 (1963) 1743-1748.

[17] K. Kakushima, T. Bourouina, T. Sarnet, G. Kerrien, D. Débarre, J. Boulmer, H. Fujita, Microelectronics Journal 36 (2005) 629-633.

[18] G.Kerrien, J. Boulmer, D. Débarre, D. Bouchier, A. Grouillet, D. Lenoble, Applied Surface Science 186 (2002) 45.

[19] J. D. Plummer, M. D. Deal, P. B. Griffin, Silicon VLSI Technology: Fundamentals, Practice and Modeling (2000) 376.

ACKNOWLEDGEMENTS

This work was supported by the S-LoTTuSS project through the grant agreement PTDC/CTM-CTM/28962/2017, financed by national funds FCT/MCTES (PIDDAC), and by FCT – Project UIDB/50019/2020 – IDL – Instituto Dom Luiz.

The authors acknowledge use of facilities and the assistance of Dr. KEITH YENDALL in the Loughborough Materials Characterisation Centre, as well as the support from The Research Council of Norway (RCN) through Project No. 239895/F20.